

Integrated magnonic half-adder

Qi Wang¹, Roman Verba², Thomas Brächer¹, Philipp Pirro¹, and Andrii V. Chumak^{1}*

¹Faculty of Physics and Research Center OPTIMAS, University of Kaiserslautern, Kaiserslautern 67663, Germany

²Institute of Magnetism, Kyiv 03680, Ukraine

Spin waves and their quanta magnons open up a promising branch of high-speed and low-power information processing. Several important milestones were achieved recently in the realization of separate magnonic data processing units including logic gates, a magnon transistor and units for non-Boolean computing. Nevertheless, the realization of an integrated magnonic circuit consisting of at least two logic gates and suitable for further integration is still an unresolved challenge. Here we demonstrate such an integrated circuit numerically on the example of a magnonic half-adder. Its key element is a nonlinear directional coupler serving as combined XOR and AND logic gate that utilizes the dependence of the spin wave dispersion on its amplitude. The circuit constitutes of only three planar nano-waveguides and processes all information within the magnon domain. Benchmarking of the proposed device is performed showing the potential for sub-aJ energy consumption per operation.

146 words from 150

A spin wave (SW) is a collective excitation of the magnetic order in magnetic materials that can propagate in both conducting and insulating media. Spin waves and their quanta magnons are considered as a potential data carrier for more-than-Moore computing [1-4]. This is due to their ultrashort wavelengths in the micro- to nanometer range [5-7] in the microwave and THz frequency range [8,9], due to their ultralow losses and the absence of Joule heating [10,11], resulting in long-propagation distances of spin information [12,13], as well as because of their abundant nonlinear phenomena [14-16]. These factors make spin wave highly attractive for wave-based computing concepts [17-28]. Separate spin wave logic gates [17-20], wave-based majority gates [21-24], transistors [15,25,26] and building blocks for unconventional computing [27-30] have already been proposed in experiments or micromagnetic simulations. Thus,

* Corresponding author. Email: chumak@physik.uni-kl.de

the next step is the realization of integrated magnonic circuits consisting of at least two elements that are suitable for further integration and interconnection with other magnonic components. In general, there are two approaches to realize magnonic circuits. One is the development of magnonic circuits using magnetoelectric cells [31-33] and modern spintronics structures [4,34-36] that behave as transducers converting information between magnons and electrons. This concept suffers from the large number of required conversions from spin to charge and vice versa, which have been identified as a serious bottleneck, in particular due to the relatively low conversion efficiencies achieved so far [31]. The second approach is based on the development of all-magnon circuits in which one magnonic gate is directly controlled by the magnons from the output of another magnonic gate without any intermediate conversion to electric signal [15].

Here, we demonstrate such an integrated magnonic circuit on the example of a half-adder built from two logic gates by means of micromagnetic simulations. The magnonic half-adder has a strikingly simple design, consisting of two directional couplers [37]: The first one works in a linear regime and acts as a symmetric power splitter for each of the two inputs. The second coupler operates in a nonlinear regime and simultaneously performs XOR and AND logic operations.

Magnonic half-adder design. A general schematic layout of a half-adder in electronics is shown in Fig. 1a. It combines an XOR logic gate and an AND logic gate using three-dimensional bridge constructions. The half-adder is an essential primary component of any arithmetic logic systems, which is why we chose it as proof of concept device for an integrated magnonic circuit. It adds two single binary digital Inputs “*A*” and “*B*” and has two Outputs, sum (“*S*”) and carry (“*C*”). The truth table of a half-adder is shown in Fig. 1b.

The design of the proposed magnonic half-adder is not a direct reproduction of a complementary metal oxide semiconductor (CMOS) half-adder in the spin wave domain. It uses advantages proposed by SW physics and is based on the combination of two directional couplers [37-39] operating in different regimes and performing different functionalities. The sketch of the device is shown in Fig. 1c. Directional Coupler 1 in the magnonic half-adder acts as a power splitter for each of the two inputs and, at the same time, replaces the three-dimensional bridge [37] required for sending the signals from Input “*A*” to the gate AND and from Input “*B*” to the gate XOR (see

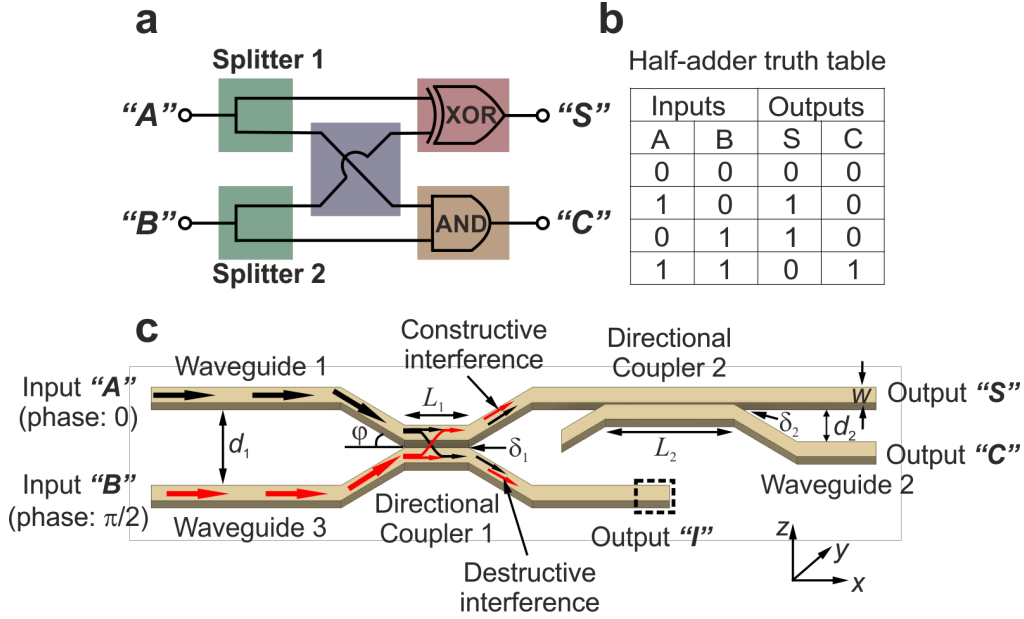


Fig. 1 The operational principle of the magnonic half-adder. **a** Sketch of half-adder in electronics. Building blocks are highlighted by different colors. **b** Half-adder truth table. **c** Schematic view of the magnonic half-adder. In this work we consider the following parameters: The widths of the YIG waveguides are $w = 100$ nm, thicknesses are $h = 30$ nm, edge to edge distances between different waveguides are $d_1 = 450$ nm, $d_2 = 210$ nm, the angles between the waveguides are $\phi = 20^\circ$, the gaps between the coupled waveguides are $\delta_1 = 50$ nm, $\delta_2 = 10$ nm, and the lengths of the coupled waveguides are $L_1 = 370$ nm and $L_2 = 3$ μ m. The arrows show the magnons flow path from inputs to logic gates.

Fig. 1a). The spin wave flow paths in the magnonic half-adder are shown by the black and red arrows in Fig. 1c: Spin waves from both inputs are split into two identical spin waves of half intensity by the Directional Coupler 1. One pair of the waves is directed to the Directional Coupler 2 via the Waveguide 1 and the other pair is guided into the idle Output “P” via the Waveguide 3. In the present simulation, the Output “P” just features a high damping region at the end (shown in the figure with a dashed rectangle) and it does not contribute to the half-adding function. However, it acts as a XOR logic gate and, potentially, it could be used in addition to the half-adder function of the device. The Directional Coupler 2 performs the actual half-adder operation and its operational principle is described in the next section.

The material we use for the numerical simulations is Yttrium Iron Garnet (YIG) which features the smallest today’s known SW losses together with large velocities of short-wavelength exchange spin waves [6,10,11,13]. One of the greatest advantage of magnon-based data processing systems is their scalability, since the smallest wavelength is limited by the lattice constant of the used magnetic material. In our

simulations we have chosen the minimal width of the waveguides to be 100 nm (see Fig. 1 for the sizes of the structure) which can be reliably fabricated using modern patterning techniques [12,40-43]. The properties of spin waves in such nano-scaled waveguides were studied analytically, numerically and experimentally in Ref. [43].

Theoretical model of the nonlinear directional coupler. The processing of data, in general, requires the utilization of elements with nonlinear characteristics that are, e.g., provided by a semiconductor transistor in CMOS. Spin waves possess a variety of natural and very pronounced nonlinear phenomena [44] that potentially can be used for computing such as four-magnon scattering, which was, for instance, used in the demonstration of the first magnon transistor [15]. Here, we utilize the phenomenon of the nonlinear dependence of SW frequency on its amplitude [44,45]. The increase in the SW amplitude results in a shift of the SW dispersion and in a phase accumulation due to the change in SW wavelength while conserving its frequency. The utilization of this phenomenon for data processing has the advantage that, unlike in the magnon scattering-based approaches, no magnon energy is lost to idle magnons generated due to the scattering [15].

The basic configuration of the directional coupler consists of dipolarly-coupled straight parallel waveguides and of bent waveguides in order to guide spin waves in and out – see Fig. 2a. Directional couplers operating in the linear regime were comprehensively studied e.g. in optics and in magnonics [37,38]. A power dependence of the characteristics of SW-based directional couplers was observed in experiments and simulations on mm-scale samples by Sadovnikov, et al. [16,39].

When two parallel magnetic SW waveguides are placed sufficiently close to each other, the dipolar coupling between them results in a splitting of the dispersion curve of the isolated waveguides into symmetric and antisymmetric modes of the coupled waveguides [37,38]. The analytically calculated [37] dispersion relation of the isolated SW waveguide is shown in Fig. 2b by the grey solid line for the case of the lowest SW mode with a quasi-uniform profile across the waveguide width [43]. The split dispersion relations in the linear regime in the coupled waveguides are shown in the figure by the blue lines. To obtain the linear dispersion, small SW amplitudes are excited by a microwave field of $h_{rf} = 2$ mT. When the excited SW frequencies are above the minimum frequency of the antisymmetric mode (about 2.278 GHz), the symmetric and antisymmetric SW modes with different wavenumber k_s and k_{as} will be

excited simultaneously in the coupled waveguides. The constructive and destructive interferences of these two propagating SW modes results in a periodic energy exchange between the two waveguides. In doing so, the spin waves excited in one of the waveguides transfer their energy to the other after propagation over a certain distance which is called the coupling length L_C . The coupling length L_C can be calculated as $L_C = \pi / \Delta k_x = \pi / |k_s - k_{as}|$ and depends on various parameters such as the SW wavelength, the applied magnetic field, the geometrical sizes of the waveguides and their magnetizations [16,37-39].

The output power in the first waveguide normalized by the total power $P_{1out}/(P_{1out}+P_{2out})$ can be expressed using the characteristic coupling length L_{C2} :

$$\frac{P_{1out}}{P_{1out} + P_{2out}} = \cos^2\left(\pi L_2 / (2L_{C2})\right), \quad (1)$$

where $L_2 = 3 \mu\text{m}$ is the length of the coupled waveguide in the Directional Coupler 2. Figure 2c shows the normalized output power in the first waveguide as a function of the SW frequency f in the frequency range from 2.28 GHz to 2.65 GHz. The result of numerical simulations in the linear regime is shown with the blue symbols and the analytic calculation with the blue solid lines (see Methods for details). One can clearly see, that the output power P_{1out} strongly depends on the SW frequency. This is due to the strong dependence of the coupling length L_{C2} on the SW wavenumber [37,38]. The coupling length, consequently, defines the energy distribution between the output waveguides for a given length of the coupled waveguides. The small mismatch between simulations and theory in the region below 2.3 GHz is mainly caused by the damping, which is not taken into account in the theory, and by the large sensitivity of the coupling coefficient to the dispersion of the antisymmetric mode, which is practically flat in this region.

When the input SW power increases, nonlinear effects start to play an important role. In the range of relatively weak nonlinearity, the main impact is produced by the nonlinear frequency shift of the SW [16,39,44,45]. Since the dipolar coupling between waveguides is much smaller than the internal forces, i.e., the splitting of the collective SW modes is much lesser than the SW frequency, we can neglect a nonlinear correction to the coupling strength. In this case, the power-dependent SW dispersion of the collective modes of coupled waveguides can be calculated as [46]:

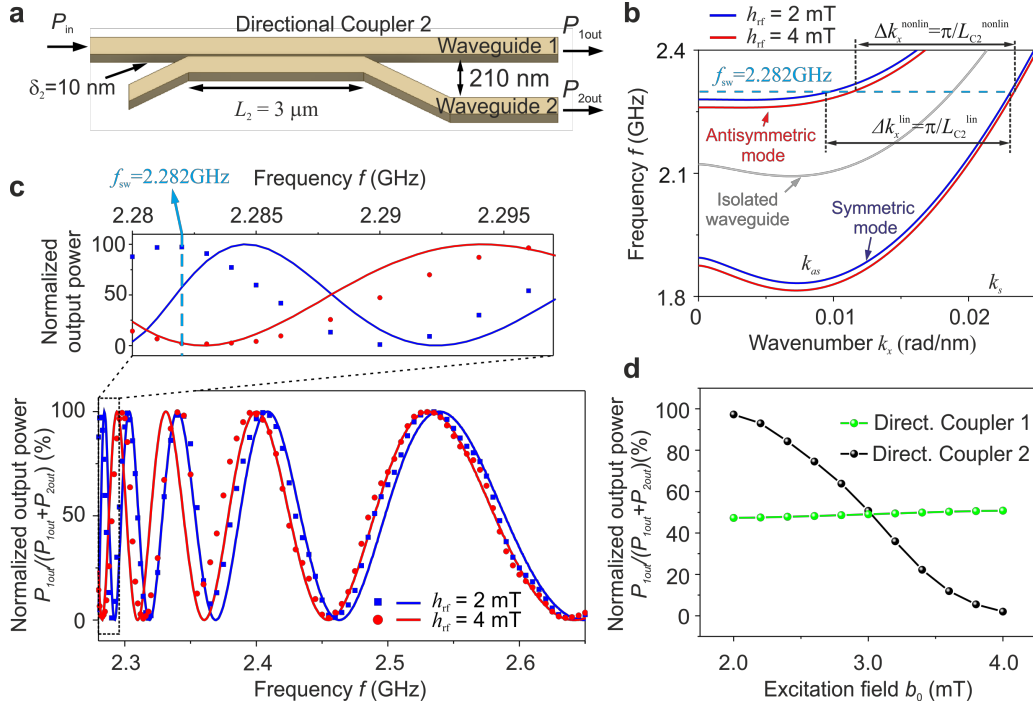


Fig. 2 Modeling and characteristics of the Directional Coupler 2. **a** Schematic of the directional coupler. **b** Analytically-calculated dispersion curves for the coupled waveguides for small (blue lines) and large (red lines) excitation fields h_{rf} . The change in the coupling length L_{C2} is clearly visible that is associated with the decrease in the SW frequency with the increase in its amplitude. **c** Normalized output power in the first waveguide $P_{1out}/(P_{1out}+P_{2out})$ as a function of frequencies for different excitation field h_{rf} (symbols - simulations, lines – analytic theory). A zoom of the region marked with the dashed rectangle is shown in the top panel. **d** Simulated normalized output power P_{1out} as a function of the excitation field b_0 for a fixed frequency of $f = 2.282$ GHz for Directional Coupler 1 and 2.

$$f_{s,as}^{(nl)}(k_x, a_{k_x}) = f_{s,as}^{(0)}(k_x) + T_{k_x} |a_{k_x}|^2 \quad (2)$$

where $f_{s,as}^{(0)}(k_x)$ are the dispersion relations of symmetric and antisymmetric modes of the coupled waveguides in the linear regime, a_{k_x} is the dimensionless SW amplitude and T_{k_x} the nonlinear frequency shift of SWs in an isolated waveguide. This frequency shift is mainly due to the decrease in the effective magnetization of a magnetic material with the increase in the magnetization precession angle [44,45]. All these characteristics are described in more detail in the Methods Section. For the further calculations, we used the numerically found relation between the excitation field and the amplitude of the dynamic magnetization with both in units of mT. In in-plane magnetized structures the nonlinear shift is negative [46] and, thus, according to

Eq. (2), the SW dispersion shifts down with an increase in SW amplitude – see red lines in Fig. 2b. Thus, a fixed SW frequency of 2.282 GHz becomes correspondent to different SW wavenumbers what changes the parameter $\Delta k_x = \pi/L_{C2}$ from Δk_x^{lin} to $\Delta k_x^{\text{nonlin}}$ (see red dots and lines in Fig. 2) with an increase in the excitation field from $b_0 = 2$ mT to 4 mT. Consequently, the coupling length L_{C2} of the directional coupler also changes.

The power dependence of the output of Directional Coupler 2 by assuming that input spin waves arrive in the first waveguide only and by using the Taylor expansion of the frequency dependence of the coupling length, can be found to:

$$\frac{P_{1\text{out}}}{P_{1\text{out}} + P_{2\text{out}}} = \cos^2 \left(\frac{\pi L_2}{2L_{C2}^{\text{lin}}} - \frac{L_2}{L_{C2}^{\text{lin}}} \frac{\pi}{2L_{C2}^{\text{lin}}} \frac{\partial L_{C2}}{\partial f} T_{k_x} \left| a_{k_x} \right|^2 \right) \quad (3)$$

The power-independent term is proportional to the ratio of the directional coupler length to the coupling length in the linear regime L_2/L_{C2}^{lin} . The output power $P_{1\text{out}}$ periodically changes with a change in the coupling length and is maximal for the cases $L_2/L_{C2}^{\text{lin}} = 0, 2, 4, \dots$ (see Fig. 2c). Simultaneously, as it is seen from Eq. (3), the sensitivity to the nonlinear effect increases with the increase in the ratio L_2/L_{C2}^{lin} . Therefore, the longer the directional coupler is and the more coupling lengths it spans, the higher is the nonlinear phase accumulation. This is the reason why the Directional Coupler 2 in our half-adder design is long and features a strong coupling provided by the small gap between the waveguides of only 10 nm. It has a length of $L_2 = 14 L_{C2}^{\text{lin}}$ and it is very sensitive to the increase in the SW amplitude passing through it. As a result, a complete energy transfer from Output 1 to Output 2 is observed in the micromagnetic simulations if the SW amplitude is increased by a factor of two ($L_2 = 13 L_{C2}^{\text{nonlin}}$) – see black line in Fig. 2d. The normalized output SW power in the first waveguide decreases from 97.3% at $b_0 = 2$ mT to 2.0% at $b_0 = 4$ mT. Due to this nonlinear switching effect, the Directional Coupler 2 performs a combined AND and XOR logic function, as will be described in the following.

At the same time, the first Directional Coupler 1 in the half-adder design should remain in the linear regime and its coupling length should be independent on the SW amplitude. This is achieved by its smaller length of 370 nm as well as by a decreased strength of the coupling via an increased spacing between the waveguides of 50 nm. As a result, Directional Coupler 1 spans only half of the coupling length $L_1 = 0.5L_{C1}^{\text{lin}}$. Thus, it requires much higher SW amplitudes to show a power dependence and in our

working range of SW amplitudes, its output remains around 50% and is independent on the excitation field – see green symbols in Fig. 2d. Hence, in contrast to Directional

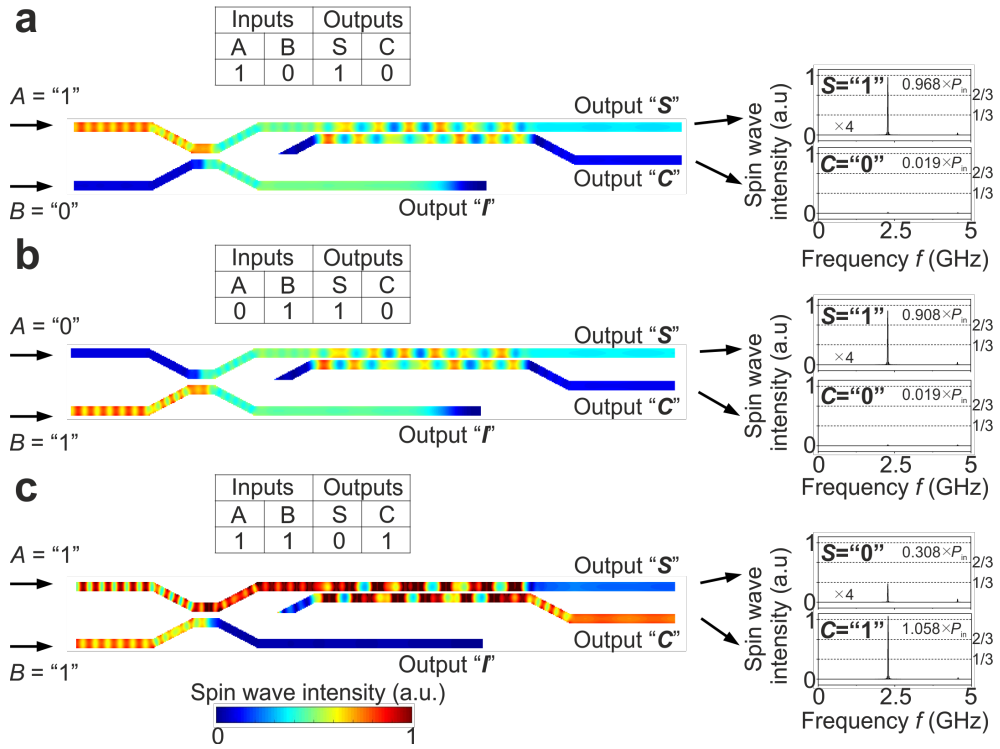


Fig. 3 Operational principle of the magnonic half-adder. The SW intensity distributions for different inputs combinations: **a** “A” = “1”, “B” = “0”, **b** “A” = “0”, “B” = “1” and **c** “A” = “1”, “B” = “1”. The truth tables for each inputs combinations are shown on the top of the structure. The normalized output SW intensities in the outputs are shown on the right side. All the outputs “S” are multiplied by a factor of four.

Coupler 2, Directional Coupler 1 works as a stable energy splitter, combiner and bridge for the two input signals.

Operational principle of the magnonic half-adder. The operational principle of the half-adder is shown in Fig. 3. Binary data is coded into the SW amplitude, namely, in the ideal case, a spin wave of a given amplitude (e.g., $M_z/M_s = 0.057$) corresponds to the logic state “1” while zero SW amplitude corresponds to “0”. In the following, we normalize all output SW intensity to the input SW intensity. In the more realistic cases considered below, we utilize an approach from CMOS: a normalized SW intensity below 1/3 is considered to be logic “0” and above 2/3, it is logic “1”.

The operational principle of the half-adder is as follows. Let us first consider the case of logic inputs “A” = “1” and “B” = “0” – see Fig. 3a. In this case, the SW injected into

the Input “ A ” is split into two equal parts by the Directional Coupler 1. One of them is directly guided to the Directional Coupler 2 by the upper conduit. The SW intensity is chosen in such a way that Directional Coupler 2 remains in the linear regime ($L_{C2}^{\text{lin}} \approx 214 \text{ nm} \approx 14/L_2$) and after initial oscillations, the SW is guided into the Output “ S ” as shown in the figure. Only about 1.9% of the SW energy goes into the Output “ C ”. This corresponds to the logic Outputs “ S ” = “1” and “ C ” = “0”. If a SW is injected in Input “ B ” only, this corresponds to the logic inputs “ A ” = “0” and “ B ” = “1” – see Fig. 3b. The situation in this case is quite similar to the previous one: The SW intensity is split into two parts by the Directional Coupler 1, one of which is guided to the output “ S ” via the Directional Coupler 2 and, thus, again “ S ” = “1”, “ C ” = “0”. The situation is different for the input logics states “ A ” = “1” and “ B ” = “1” – see Fig. 3c. It is assumed that the phase of the SW injected into the Input “ B ” is shifted by $\pi/2$ with respect to the one in the Input “ A ” in order to compensate the $-\pi/2$ phase shift caused by the Directional Coupler 1. In practice, this can be easily realized by varying, for instance, the length of the magnonic conduits between two half-adders in series. As a result, the excitation of SWs in both inputs results in their constructive interference and in a twice larger SW amplitude arriving at Directional Coupler 2. As was discussed above, this increase in the SW intensity switches the coupler to the nonlinear regime ($L_{C2}^{\text{nonlin}} \approx 230 \text{ nm} \approx 13/L_2$) and the spin wave is guided to the output “ C ”. This corresponds to the logic Outputs “ S ” = “0” and “ C ” = “1” (see Fig. 3c) and, thus, the whole truth-table of the half-adder is realized. The combination of two directional couplers performs the AND and XOR logic functions due to the phenomenon of nonlinear SW frequency shift.

Please note that the all-magnon circuit concept [15] requires that the signal from the output of a magnonics gate can be directly guided into the input of the next one. In order to satisfy this condition, the spin wave intensity at the Outputs “ S ” still has to be amplified by a factor of four due to the energy splitting in the Directional Coupler 1 and due to parasitic reflections and spin-wave damping in the waveguides. The output signals “ S ” shown in Fig. 3 are artificially multiplied by 4. The most promising realization of such an amplifier is based on the utilization of parametric pumping [47,48] or the spin Hall effect (SHE) in combination with Spin Transfer Torque (STT) [4, 10, 49]. In contrast, the SW amplitude in the output “ C ” is either vanishingly small or is approximately equal to the input SW amplitude as a consequence of constructive interference. Thus, no amplifier is required for the “Carry” output of the half-adder.

Discussion

At the final part of this paper, we would like to discuss scalability, operational frequency and potential power consumption of the presented magnonic half-adder. The summary of these parameters is shown in Table 1. Parameters for two different devices are estimated: The first one is the device which was simulated and discussed above. The width of the YIG waveguides is equal to 100 nm and can be reliably fabricated according to the recent achievements [43]. The second device is an estimation performed for a device with a width of the waveguides of 10 nm and with YIG being replaced by CoFeB, a commonly used metallic ferromagnet in spintronics applications (parameters: $M_s = 13.5 \times 10^5$ A/m, $A = 15$ pJ/m [50]). In addition, the SW wavelength was decreased to 50 nm and the SW frequency was increased to 31 GHz. The second device was not simulated but the estimation was performed on the basis of the known scalability of the proposed approach. It has to be mentioned that the second device does not constitute a fundamental limit but is merely an estimation based on the current state of the art of fabrication technology, since CMOS technology reported on the industrial production of devices with below 10 nm minimal size. A further improvement in all characteristics by about 10 times is potentially achievable.

Parameters	YIG (100 nm)	CoFeB (10nm)
SW frequency (GHz)	2.282	31
SW wavelength (nm)	340	50
SW group velocity (m/s)	25	700
Delay time (ns)	150	1.14
Operational speed (MHz)	2.2	300
Area (μm^2)	3.9	0.056
Energy consumption (aJ/oper.)	24.6	0.187

Table 1. Characteristics of the half-adder investigated in the paper and estimated characteristics of a device miniaturized down to 10 nm minimal size.

According to the table, the area of the simulated half-adder is $3.9 \mu\text{m}^2$ and is, thus, only few times larger than a corresponding CMOS device containing 14 transistors. In contrast to a CMOS realization, the magnonic half-adder consist of only one material and of only one planar layer. This drastically simplifies its fabrication and decreases

its potential costs. The area can be readily decreased down to $0.056 \mu\text{m}^2$ for the second device. This significant decrease in the footprint of the computing device with respect to CMOS technology arises from the usage of the additional degrees of freedom for spin waves such as their phase and nonlinearity. In addition, it should be noted that the largest part of the half-adder is given by the Directional Coupler 2, which could potentially be further decreased via the utilization of other, stronger coupling mechanisms between the SW waveguides like exchange instead of dipolar coupling.

Operational speed is another important requirement. In the presented half-adder, the operating frequency is defined by the whole length of the device with respect to the SW group velocity. In our design, the SW propagation time from input to output is about 150 ns. In order to achieve a stabilization of the interference pattern and the nonlinear processes, the minimum SW pulse duration should be about 300 ns and the period between operations is about 450 ns. The latter defines the operational frequency of around 2.2 MHz. According to Table 1, the calculation time can be reduced to 1.14 ns in the miniaturized device, and its operational frequency can be increased up to 0.3 GHz.

Finally, small energy consumption of computing systems is probably the most crucial requirement taking into account the constantly increasing amount of information that has to be processed. In our simulations, we record the total energy of the device as a function of simulation time. The energy injected into the device per nanosecond is equal to 8.2×10^{-20} J/ns. For the 300 ns pulse duration the energy consumption per operation is, thus, 2.46×10^{-17} J/operation. Even without taking into account that the half-adder performs a quite complex operation, this value is more than one order of magnitude better than current CMOS values (10^{-16} J/bit [3]). The energy consumption for the miniaturized device should be especially highlighted as it is a remarkably low 1.87×10^{-19} J/operation. At the same time, we have to underline that this energy consumption is related to the energy within the magnonic domain only and it does not take into account the energy consumed during the transfer of signals between the elements and the energy required for the SW amplification.

In conclusion, we have proposed and numerically tested a magnonic half-adder that constitutes of two logic gates and is potentially suited for further integration with other logic gates relying on the same concept. In this integrated magnonic circuit, the magnons are controlled by magnons themselves without any conversion to the electric

domain which ensures low energy consumption. The half-adder consists of two directional couplers, one of which acts as a power splitter and another which acts as a nonlinear switch. The operational principle of the latter is based on the nonlinear shift of spin wave frequency with an increase in spin wave amplitude. An analytic theory is developed to describe this phenomenon and is verified numerically as well as the whole functionality of the half-adder.

In comparison to CMOS technology, the half-adder consists of three magnetic nanowires only and substitutes 14 transistors in electronics. Only one magnetic material is used, the design is fully planar and occupies one single layer. The half-adder, although being based on 100 nm technology, has characteristics comparable to a 10 nm CMOS half-adder. At the same time, the magnonic half-adder has large potential for miniaturization and further improvement. The estimation of a 10 nm-based magnonic half-adder predicts a two orders of magnitude decrease in footprint, a calculation time of around 1 ns, and a sub-aJ energy consumption per operation.

Methods

Spin wave dispersion calculation in the linear region. The details of the calculations have been fully described in our previous paper [37]. The SW dispersion curve can be obtained by solving the Landau-Lifshitz equation of magnetization dynamics in the linear approximation and neglecting the damping term. The SW dispersion relation in the isolated waveguide is given by [37]:

$$f_0(k_x) = \frac{1}{2\pi} \sqrt{\Omega^{yy} \Omega^{zz}} = \frac{1}{2\pi} \sqrt{(\omega_H + \omega_M (\lambda^2 k_x^2 + F_{k_x}^{yy}(0))) (\omega_H + \omega_M (\lambda^2 k_x^2 + F_{k_x}^{zz}(0)))} \quad (4)$$

The dispersion relation for the two coupled waveguides (two modes) is

$$f_{s,as}(k_x) = \frac{1}{2\pi} \sqrt{(\Omega^{yy} \pm \omega_M F_{k_x}^{yy}(d)) (\Omega^{zz} \pm \omega_M F_{k_x}^{zz}(d))} \quad (5)$$

where $\Omega^{ii} = \omega_H + \omega_M (\lambda^2 k_x^2 + F_{k_x}^{ii}(d))$, $i = y, z$, $\omega_H = \gamma B_{ext}$, $\omega_M = \gamma \mu_0 M_s$, M_s is the saturation magnetization, γ is the gyromagnetic ratio, μ_0 is the vacuum permeability, $\lambda = \sqrt{2A / (\mu_0 M_s^2)}$ is the exchange length, A is the exchange constant, $d = w + \delta$ is the distance between the centers of the two waveguides, δ is the gap between the two waveguides with width w . The coordinate system used is shown in Fig. 1c: The x -axis is directed along the waveguides, the z -axis is out-of-plane. The tensor $\hat{\mathbf{F}}_{k_x}$ describes the dynamical magneto-dipolar interaction [51,52]:

$$\hat{\mathbf{F}}_{k_x}(d) = \frac{1}{2\pi} \int \hat{\mathbf{N}}_k e^{ik_y d} dk_y \quad (6)$$

$$\hat{\mathbf{N}}_k = \frac{|\sigma_k|^2}{\tilde{w}} \begin{pmatrix} \frac{k_x^2}{k^2} f(kh) & \frac{k_x k_y}{k^2} f(kh) & 0 \\ \frac{k_x k_y}{k^2} f(kh) & \frac{k_y^2}{k^2} f(kh) & 0 \\ 0 & 0 & 1 - f(kh) \end{pmatrix} \quad (7)$$

where $f(kh) = 1 - (1 - \exp(-kh)) / (kh)$, $k = \sqrt{k_x^2 + k_y^2}$, h is the thickness, σ_k is the Fourier transform of the SW profile across the width of the waveguide, and \tilde{w} is the normalized constant of the mode profile. In this case, the spins are fully unpinned at the edge of the waveguides [43]. The Fourier transform is, then, described by the function $\sigma_k = w \text{sinc}(k_y w / 2)$ and $\tilde{w} = w$.

Nonlinear frequency shift. The nonlinear shift coefficient T_{k_x} in the isolated waveguide can be calculated using the framework of [53] and by assuming a uniform mode profile across the waveguide thickness and width. Accounting for the negligible static demagnetization of a waveguide along its length, $F_0^{xx} = 0$, the nonlinear shift coefficient becomes equal to [48]:

$$T_{k_x} = \left((\omega_H - A_{k_x}) + \frac{B_{k_x}^2}{2\omega_0^2} (\omega_M (4\lambda^2 k_x^2 + F_{2k_x}^{xx}(0)) + 3\omega_H) \right) / 2\pi, \quad (8)$$

where

$$A_{k_x} = \omega_H + \frac{\omega_M}{2} (2\lambda^2 k_x^2 + F_{k_x}^{yy}(0) + F_{k_x}^{zz}(0)), \quad (9)$$

$$B_{k_x} = \frac{\omega_M}{2} (F_{k_x}^{yy}(0) - F_{k_x}^{zz}(0)). \quad (10)$$

The relation between the dynamic magnetization component and the canonical SW amplitude a_{k_x} is given by:

$$M_z = M_s a_{k_x} \sqrt{2 - |a_{k_x}|^2} (u_{k_x} - v_{k_x}), \quad (11)$$

with

$$u_{k_x} = \sqrt{\frac{A_{k_x} + \omega_0}{2\omega_0}} \quad \text{and} \quad v_{k_x} = -\text{sign}[B_{k_x}] \sqrt{\frac{A_{k_x} - \omega_0}{2\omega_0}}. \quad (12)$$

Micromagnetic simulations. The micromagnetic simulations were performed by the GPU-accelerated MuMax3 [54] code. The simulated structure of the magnonic half-

adder is shown in Fig. 1c. The parameters of nanometer thick YIG are obtained from experiment and are as follows [11]: saturation magnetization $M_s = 1.4 \times 10^5$ A/m, exchange constant $A = 3.5$ pJ/m, and Gilbert damping $\alpha = 2 \times 10^{-4}$. The damping at the ends of the simulated structure and the high damping absorber is set to exponentially increase to 0.5 to prevent SW reflection [55]. The high damping region could be realized in the experiment by putting another magnetic material or metal on top of YIG to enhance the damping or it can just correspond to waves guided into further parts of the magnonic network. No external bias field is applied. The static magnetization orients itself parallel to the waveguides spontaneously due to the strong shape anisotropy in the nanoscale waveguides. The mesh was set to $10 \times 10 \times 30$ nm³. To excite propagating spin waves, a sinusoidal magnetic field $b = b_0 \sin(2\pi ft)$ is applied over an area of 100 nm in length, with a varying oscillation amplitude b_0 and the microwave frequency f . $M_z(x,y,t)$ of each cell was collected over a period of 300 ns which is long enough to reach the steady state. The fluctuation $m_z(x,y,t)$ were calculated for all cells via $m_z(x,y,t) = M_z(x,y,t) - M_z(x,y,0)$, where $M_z(x,y,0)$ corresponds to the ground state. The SW spectra of the output signals are calculated by performing a fast Fourier transformation from 250 ns to 300 ns which corresponds to the steady state.

Acknowledgements:

The authors thank Christoph Adelman and Burkard Hillebrands for support and valuable discussions. This research has been supported by ERC Starting Grant 678309 MagnonCircuits and by the DFG through the Collaborative Research Center SFB/TRR-173 “Spin+X” (Projects B01 and B04) and through the Project DU 1427/2-1. R. V. acknowledges support from the Ministry of Education and Science of Ukraine, Project 0118U004007.

References:

1. Khitun, A. Bao, M. & Wang, K. L. Magnonic logic circuits. *J. Phys. D Appl. Phys.* **43**, 264005 (2010).
2. Lenk, B. *et al.* The building blocks of magnonics. *Phys. Rep.* **507**, 107-136 (2011).
3. Nikonov, D. E. & Young, I. A., Overview of beyond-CMOS devices and a uniform methodology for their benchmarking. *Proc. IEEE* **101**, 2498-2533 (2013).
4. Chumak, A. V., *et al.* Magnon spintronics. *Nat. Phys.* **11**, 453-461 (2015).

5. Wintz, S. *et al.* Magnetic vortex cores as tunable spin-wave emitters, *Nat. Nano.*, **11**, 948-953 (2016).
6. Yu, H., *et al.* Approaching soft x-ray wavelengths in nanomagnet-based microwave technology. *Nat. Commun.* **7**, 11255 (2016).
7. Brächer, T. *et al.* Detection of short-waved spin waves in individual microscopic spin-wave waveguides using the inverse spin hall effect. *Nano Lett.* **17**, 7234-7241 (2017).
8. Kampfrath, T. *et al.* Coherent terahertz control of antiferromagnetic spin waves. *Nature Photon.* **5**, 31-34 (2011).
9. Balashov, T. *et al.* Magnon dispersion in thin magnetic films *J. Phys.: Condens. Matter*, **26**, 394007 (2014).
10. Kajiwara, Y. *et al.* Transmission of electrical signals by spin-wave interconversion in a magnetic insulator. *Nature* **464**, 262-266 (2010).
11. Dubs, C. *et al.* Sub-micrometer yttrium iron garnet LPE films with low ferromagnetic resonance losses. *J. Phys. D Appl. Phys.* **50**, 204005 (2017).
12. Pirro, P. *et al.* Spin-wave excitation and propagation in microstructured waveguides of yttrium iron garnet/Pt bilayers. *Appl. Phys. Lett.* **104**, 012402 (2014).
13. Yu, H. *et al.* Magnetic thin-film insulator with ultra-low spin wave damping for coherent nanomagnonics. *Sci. Rep.* **4**, 6848 (2014).
14. Demidov, V. E. *et al.* Nonlinear propagation of spin waves in microscopic magnetic stripes. *Phys. Rev. Lett.* **102**, 177207 (2009).
15. Chumak, A. V., Serga, A. A., & Hillebrands, B. Magnon transistor for all-magnon data processing. *Nat. Commun.* **5**, 4700 (2014).
16. Sadovnikov, A. V. *et al.* Nonlinear spin wave coupling in adjacent magnonic crystals. *Appl. Phys. Lett.* **109**, 042407 (2016).
17. Schneider, T., Serga, A. A. & Hillebrands, B. Realization of spin-wave logic gate. *Appl. Phys. Lett.*, **92**, 022505 (2008).
18. Lee, K. -S. *et al.* Conceptual design of spin wave logic gates based on a Mach-Zehnder-type spin wave interferometer for universal logic functions. *J. Appl. Phys.* **104**, 053909 (2008).
19. Jamali, M. *et al.* Spin wave nonreciprocity for logic device applications. *Sci. Rep.* **3**, 3160 (2013).
20. Zografos, O. *et al.* Exchange-driven magnetic logic. *Sci. Rep.* **7**, 12154 (2017).
21. Khitun, A. & Wang, K. L. Non-volatile magnonic logic circuits engineering. *J. App. Phys.* **110**, 034306 (2011).

22. Klingler, S. *et al.* Design of a spin-wave majority gate employing mode selection. *Appl. Phys. Lett.* **105**, 152410 (2014).
23. Radu, I. P. *et al.* Spintronic majority gates. in 2015 IEEE International Electron Devices Meeting (IEDM), pp. 32.5.1-32.5.4, 2015.
24. Fischer, T. *et al.* Experimental prototype of a spin-wave majority gate. *Appl. Phys. Lett.* **110**, 152401 (2017).
25. Wu, H. *et al.* Magnon valve effect between two magnetic insulators. *Phys. Rev. Lett.* **120**, 097205 (2018).
26. Cramer, J. *et al.* Magnon detection using a ferroic collinear multilayer spin valve. *Nat. Comm.* **9**, 1089 (2018)
27. Torrejon, J. *et al.* Neuromorphic computing with nanoscale spintronic oscillators. *Nat. Nano.* **547**, 428-431 (2017).
28. Brächer, T. & Pirro, P. An analog magnon adder for all-magnonic neurons. *J. Appl. Phys.* **124**, 152119 (2018).
29. Kozhevnikov, A. *et al.* Pattern recognition with magnonic holographic memory device. *Appl. Phys. Lett.* **106**, 142409 (2015).
30. Papp, Á. *et al.* Nanoscale spectrum analyzer based on spin-wave interference. *Sci. Rep.* **7**, 9245 (2017).
31. Cherepov, S. *et al.* Electric-field-induced spin wave generation using multiferroic magnetoelectric cells. *Appl. Phys. Lett.* **104**, 082403 (2014).
32. Dutta, S. *et al.* Non-Volatile clocked spin wave interconnect for beyond-CMOS nanomagnet pipelines. *Sci. Rep.* **5**, 09861 (2015).
33. Duflou, R. *et al.* Micromagnetic simulations of magnetoelastic spin wave excitation in scaled magnetic waveguides. *Appl. Phys. Lett.* **111**, 192411 (2017).
34. Sandweg, C. W. *et al.* Spin pumping by parametrically excited exchange magnons. *Phys. Rev. Lett.* **106**, 216601 (2011).
35. Collet, M. *et al.* Generation of coherent spin-wave modes in yttrium iron garnet microdiscs by spin-orbit torque. *Nat. Comm.* **7**, 10377 (2016).
36. Talmelli, G. *et al.* Spin-wave emission by spin-orbit-torque antennas. *Phy. Rev. Appl.* **10**, 044060 (2018).
37. Wang, Q. *et al.* Reconfigurable nanoscale spin-wave directional coupler. *Sci. Adv.* **4**, e1701517 (2018).
38. Sadovnikov, A. V. *et al.* Directional multimode coupler for planar magnonics: Side-coupled magnetic stripes. *Appl. Phys. Lett.* **107**, 202405 (2015).

39. Sadovnikov, A. V. *et al.* Toward nonlinear magnonics: Intensity-dependent spin-wave switching in insulating side-coupled magnetic stripes. *Phys. Rev. B* **96**, 144428 (2017).
40. Duan, Z. *et al.* Nanowire spin torque oscillator driven by spin orbit torques. *Nat. Comm.* **5**, 5616 (2014).
41. Collet, M. *et al.* Generation of coherent spin-wave modes in yttrium iron garnet microdiscs by spin-orbit torque. *Nat. Commun.* **7**, 10377 (2016).
42. Schneider, M. *et al.* Bose-Einstein condensation of quasi-particles by rapid cooling. *arXiv:1612.07305*.
43. Wang, Q. *et al.* Spin pinning and spin-wave dispersion in nanoscopic ferromagnetic waveguides. *arXiv:1807.01358*.
44. Gurevich, A. G. & Melkov, G. A. Magnetization oscillations and waves (CRC-press, London, New York, 1996).
45. Bauer, H. G. *et al.* Nonlinear spin-wave excitations at low magnetic bias fields. *Nat. Comm.* **6**, 8274 (2015).
46. Verba, R. *et al.* Excitation of propagating spin waves in ferromagnetic nanowires by microwave voltage-controlled magnetic anisotropy. *Sci. Rep.* **6**, 25018 (2016).
47. Brächer, T., Pirro, P. & Hillebrands, B. Parallel pumping for magnon spintronics: Amplification and manipulation of magnon spin currents on the micron-scale. *Phys. Rep.* **699**, 1-34 (2017).
48. Verba, R. *et al.* Amplification and stabilization of large-amplitude propagating spin waves by parametric pumping. *App. Phys. Lett.* **112**, 042402 (2018).
49. Evelt, M. *et al.* High-efficiency control of spin-wave propagation in ultra-thin yttrium iron garnet by the spin-orbit torque. *Appl. Phys. Lett.* **108**, 172406 (2016).
50. Conca, A. *et al.* Annealing influence on the Gilbert damping parameter and the exchange constant of CoFeB thin films. *Appl. Phys. Lett.* **104**, 182407 (2014).
51. Verba, R. *et al.* Collective spin-wave excitations in a two-dimensional array of coupled magnetic nanodots. *Phys. Rev. B* **85**, 014427 (2012).
52. Beleggia, M. *et al.* On the magnetostatic interactions between nanoparticles of arbitrary shape. *J. Magn. Magn. Mater.* **278**, 270-284 (2004).
53. Krivosik, P. & Patton, C. E. Hamiltonian formulation of nonlinear spin-wave dynamics: Theory and applications. *Phys. Rev. B* **82**, 184428 (2010).
54. Vansteenkiste, A. *et al.* The design and verification of MuMax3. *AIP Adv.* **4**, 107133 (2014).

55. Venkat, G. Fangohr, H. & Prabhakar, A. Absorbing boundary layers for spin wave micromagnetics. *J. Magn. Magn. Mater.* **450**, 34-39 (2018).